

# Deformation analysis of the Alqueva dam using EGMS InSAR data

Tiago Henrique, Rui Carrilho Gomes, Ana Paula Falcão

November 13, 2025

**Keywords:** Geotechnical structures behaviour, Earth observation data, Machine learning, Pattern detection, Dam monitoring

## Abstract

Understanding and predicting the behaviour of geotechnical structures is still a complex challenge. Traditional methods often fail to fully capture the complexities of these structures, which include challenges such as slope instabilities, dam behaviour, and landslides. To address these issues, significant advances have been made in Earth observation techniques, such as radar interferometry and satellite imagery, as well as in machine learning tools. These developments have provided new opportunities for monitoring and predictive modelling. This review explores the application of Earth observation techniques, such as InSAR, for detecting ground displacement and deformation. It also examines the role of machine learning in analysing large datasets, detecting patterns and anomalies, and predicting potential geotechnical failures. Despite these advancements, challenges remain, particularly regarding the reliance on high-quality data and the integration of advanced algorithms into practical applications.

## 1 Introduction

Geotechnical structures play a critical role in infrastructure and environmental management worldwide. Understanding the behaviour of these structures under varying environmental and operational conditions is essential for ensuring their safety, longevity, and performance. Dams, for example, are integral to water storage, flood control, and hydroelectric energy generation, with their stability being paramount to avoiding catastrophic failures. Over the years, traditional methods have been employed to monitor and assess the health of these structures, relying primarily on physical inspections and direct measurements. However, these methods often face limitations due to the complexity of geotechnical phenomena, such as ground deformation, structural movements, and other dynamic processes that are not easily captured using conventional techniques.

In recent years, significant advancements have been made in Earth observation technologies, including synthetic aperture radar interferometry (InSAR), satellite imagery, and remote sensing tools. These technologies provide valuable insights into the performance of geotechnical structures, allowing for the detection of ground displacement, deformations, and changes in the surrounding environment over time. Furthermore, the application of machine learning techniques has revolutionized the analysis of large and complex datasets, enabling the detection of patterns and anomalies that may indicate potential risks or structural failures.

This review aims to explore the current state of knowledge regarding the behaviour of geotechnical structures, with a particular focus on concrete dams. It delves into the role of Earth observation techniques

and machine learning in monitoring these structures, detecting early signs of potential failure, and improving predictive modelling. By reviewing recent studies, we will examine how these technologies are transforming geotechnical monitoring and providing new opportunities for risk mitigation and safety enhancement.

## 2 InSAR

### 2.1 Literature review

#### 2.1.1 Fundamentals of InSAR and Earth Observation

- Princípios físicos do radar de abertura sintética (SAR)
- Conceitos de interferometria e linha de visada (LOS)
- Tipos de órbitas: ascendente e descendente
- Erros e correções típicas (atmosfera, ruído, baseline)

The integration of advanced monitoring techniques, particularly through satellite imagery and machine learning, has revolutionized the way we study and monitor geotechnical structures. These technologies allow for real-time monitoring, better prediction of failures, and more effective intervention strategies, ensuring the safety and stability of vital infrastructure.

Recently, earth observation techniques, such as radar interferometry and satellite imagery, have become essential tools for monitoring geotechnical structures (Salcedo-Sanz et al., 2020; Simoes et al., 2021). These methods enable large-scale, continuous observation, offering valuable insights into displacement, deformation, and geohazard detection. Time-series from earth observation data are particularly useful for uncovering long-term patterns of ground displacement, providing a better understanding of subsidence and deformation processes, and enabling monitoring at a regional or even global scale. Compared to traditional in-situ methods, these techniques offer unprecedented scalability and continuity.

#### 2.1.2 Interferometric techniques and time-series approaches

- Séries temporais (SBAS, PSI)
- Aplicações em monitoramento de estruturas e movimentos do terreno
- Referências sobre decomposição vertical/horizontal

Among the most widely used techniques, Interferometric Synthetic Aperture Radar (InSAR) has gained prominence for its ability to detect ground displacement with high precision (Tomás & Li, 2017). According to Sousa et al. (2021), “Results from both the processing and analysis of a dataset of Earth observation (EO) multi-source data support the conclusion that geohazards can be identified, studied, and monitored effectively using new techniques applied to multi-source EO data.”

Within the InSAR family, several specialized techniques have been developed to enhance temporal and spatial precision. Differential InSAR (DInSAR) provides highly accurate surface deformation measurements over time, making it suitable for monitoring slow-moving geotechnical phenomena (Derauw et al., 2020). The Persistent Scatterer InSAR (PSInSAR) technique is particularly effective for detecting subtle and long-term ground movements by analysing stable reflectors that maintain coherence over time (Hariri-Ardebili et al., 2020). Meanwhile, the Small Baseline Subset (SBAS) approach minimizes spatial

and temporal baselines between image pairs, improving temporal coherence and reducing decorrelation, making it especially suitable for localized deformation studies (Park & Hong, 2021).

More recently, these methods have been extended to advanced displacement modelling and calibration workflows (Schlögl et al., 2021; Tu et al., 2023), allowing for a more robust estimation of three-dimensional ground motion and improved interpretation of geotechnical processes.

### 2.1.3 Clustering and data mining in InSAR

- Objetivo: identificar padrões espaciais ou temporais em deformações
- Métodos:
  - K-Means: agrupamento baseado em magnitudes médias
  - Hierarchical Clustering: agrupamento baseado em similaridade completa
  - Dynamic Time Warping (DTW): agrupamento de séries temporais não lineares
- Comparação entre métodos, vantagens e limitações

### 2.1.4 Applications in geotechnical monitoring

The application of InSAR-based techniques has expanded rapidly across various geotechnical domains. They have been successfully used for monitoring the structural integrity of dams, slopes, tunnels, and embankments, as well as for detecting subsidence in urban areas and mining regions.

Several studies demonstrate the effectiveness of these techniques for geotechnical monitoring: Schrögl et al. (2021) applied InSAR time-series to evaluate dam settlements; Roque et al. (2023) integrated InSAR and geomechanical modelling for slope stability assessment; and Maes (2025) explored the use of EGMS data for infrastructure deformation mapping. More recent works, such as Giordano et al. (2025), highlight the growing potential of multi-source Earth observation data and machine learning integration for predictive geohazard analysis.

## 2.2 Displacements calculation and validation

### 2.2.1 Case study overview

The case study focuses on the assessment of surface displacements obtained from the European Ground Motion Service (EGMS) and their validation against orthophoto-derived measurements. The study area corresponds to a monitored geotechnical structure — the Alqueva Dam, a double-curvature concrete arch dam located in the Alentejo region, southern Portugal. It is one of the largest dams in Western Europe, standing approximately 96 meters high with a crest length of 458 meters, forming a key element of Portugal's hydro-agricultural system. The foundation consists of green schists on the right bank and phyllites on the left bank.

The EGMS data used in this study include both ascending and descending Line-of-Sight (LOS) products, which represent ground displacements along the radar viewing direction. These LOS measurements were decomposed into vertical (Up–Down) and horizontal (East–West) components, enabling direct comparison with reference displacements derived from orthophotogrammetry (hereafter referred to as “Ortho”).

Additionally, the study employed a Digital Elevation Model (DEM) and related metadata to account for

topographic effects and to support geometric corrections. The combination of Calibrated (ascending and descending) EGMS products with ORTHO displacements allows for a comprehensive evaluation of both the vertical and horizontal deformation behavior of the structure. This integrated approach provides valuable insights into the dam's mechanical response and contributes to the validation of satellite-based ground motion measurements in complex geotechnical settings.

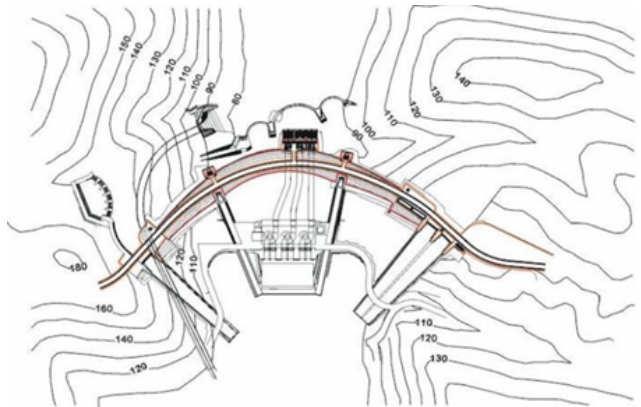


Figure 1: Views of the Alqueva Dam from different perspectives.

### 2.2.2 Decomposition of Line-of-Sight displacements

To derive the vertical ( $dV$ ) and horizontal ( $dH$ ) displacement components over the Alqueva dam, a dedicated processing workflow was implemented using Python and geospatial libraries (Pandas, GeoPandas, NumPy, SciPy). The procedure combines calibrated ascending (ASC) and descending (DESC) InSAR datasets from the EGMS Level-2b product and validates the decomposed components against the orthogonal vertical (U) and east–west (E) displacements provided by the EGMS Level-3 (ORTHO) product.

#### Data reading and spatial filtering

The calibrated ASC, DESC, and ORTHO datasets were imported into Python and spatially filtered to the dam and its immediate surroundings, defined by fixed coordinate limits in the ETRS89-LAEA (EPSG:3035) projection. This ensured consistent spatial referencing across all datasets and reduced the computational load to the relevant monitoring area.

#### Time-series reshaping

The displacement columns in the ASC, DESC, and ORTHO datasets were reshaped into a long-format table, with one row per spatial point and acquisition date. This format facilitated temporal interpolation and subsequent synchronization of datasets acquired on different dates.

#### Temporal interpolation

Since ASC and DESC acquisitions are collected on distinct dates, a common set of monthly timestamps was defined. Linear interpolation was applied to generate displacement values for both orbits at the same epoch. This ensured temporal consistency and enabled direct comparison between ASC and DESC measurements.

#### Spatial interpolation (IDW)

Since ASC and DESC pixels are not spatially coincident, the DESC displacements were interpolated onto the ASC grid using Inverse Distance Weighting (IDW). For each ASC point, the interpolation used the

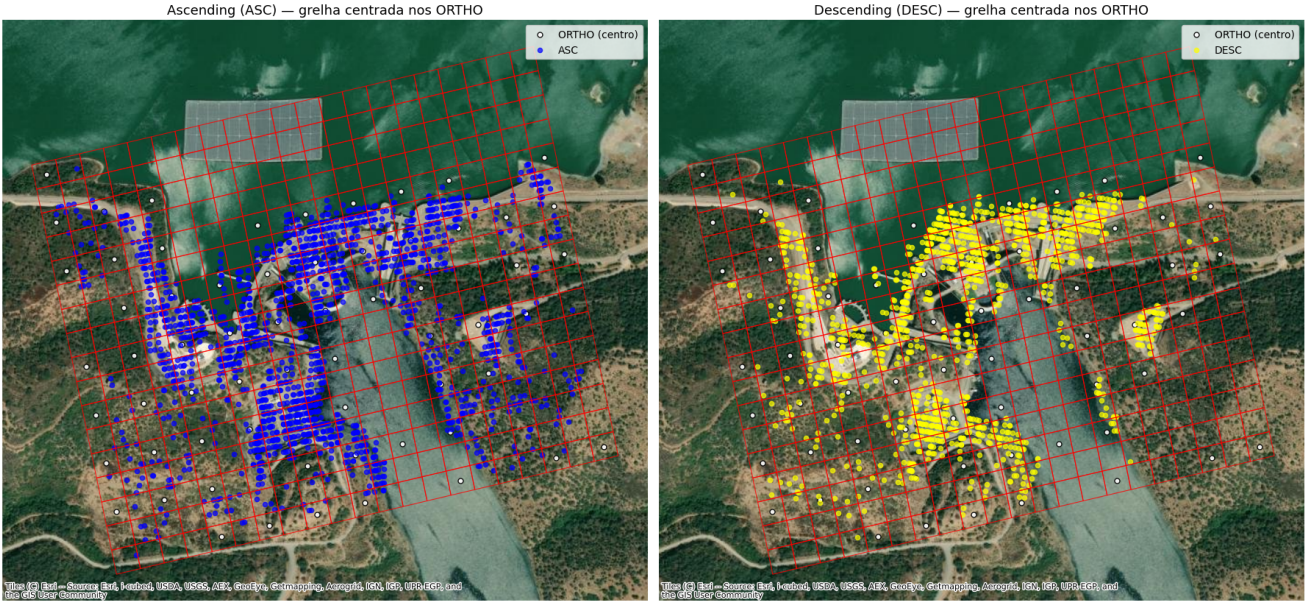


Figure 2: View of the dam and initial ASC/DESC point distribution maps illustrate the area of interest and the spatial coverage of the datasets.

five nearest DESC neighbours within a 150 m radius, weighted by the inverse square of their distance. This step also interpolated the incidence angle ( $\theta$ ) and track angle ( $\phi$ ) from the DESC geometry, ensuring that both ASC and DESC values correspond to the same ground location.



Figure 3: VMap of grid cells and points after IDW interpolation, showing the spatial alignment of ASC and DESC points.

## Computation of geometric parameters ( $\beta$ and $\gamma$ )

Two auxiliary geometric parameters are defined for each interpolated ascending (ASC) point:

- $\beta$  (orbital-geometry term) — computed as:

$$\beta = \arcsin(\cos(I) \cdot \cos(\text{latitude})) \quad (1)$$

where  $I = 98.6^\circ$  is the Sentinel-1 orbit inclination. In this work,  $\beta$  is used as a geometric correction term derived from the satellite orbital inclination and the point latitude. It is not a direct measurement of terrain slope aspect (i.e., not DEM-derived). It accounts for the relative orientation between the satellite orbit plane and the local observation latitude, consistent with the trigonometric formulation implemented in the processing code.

- $\gamma$  (cross-track tilt) — represents the local topographic tilt perpendicular to the radar line-of-sight. Given the relatively flat topography of the dam area,  $\gamma$  was set to zero ( $\gamma = 0$ ), which simplifies the decomposition while introducing negligible error for this site.

*Note:* If a DEM-based local slope/aspect correction were applied,  $\beta$  would be replaced or augmented by the DEM-derived slope aspect, and  $\gamma$  by the DEM-derived cross-track tilt. In this study, those DEM corrections were not used.

## Decomposition of Line-of-Sight (LOS) displacements into vertical and horizontal components

Let  $d_{\text{ASC}}$  and  $d_{\text{DESC}}$  be the LOS displacements from ascending and descending passes, respectively. Let  $\theta_A, \theta_D$  be the local incidence angles (angle between LOS and vertical) for ASC and DESC, and  $\alpha_A, \alpha_D$  their respective orbit azimuth (track) angles.

The LOS measurements relate to the vertical and east–west horizontal components via:

$$\begin{cases} d_{\text{ASC}} = -d_V \cos \theta_A + d_H \sin \theta_A \cos(\alpha_A + \beta + \gamma) \\ d_{\text{DESC}} = -d_V \cos \theta_D + d_H \sin \theta_D \cos(\alpha_D + \beta + \gamma) \end{cases} \quad (2)$$

Solving this  $2 \times 2$  trigonometric system yields the vertical and horizontal components:

$$d_V = \frac{d_{\text{DESC}} \sin \theta_A \cos(\beta - \gamma) + d_{\text{ASC}} \sin \theta_D \cos(\beta + \gamma)}{\cos \theta_A \sin \theta_D \cos(\beta - \gamma) + \cos \theta_D \sin \theta_A \cos(\beta + \gamma)} \quad (3)$$

$$d_H = \frac{d_{\text{DESC}} \cos \theta_A - d_{\text{ASC}} \cos \theta_D}{\cos \theta_A \sin \theta_D \cos(\beta - \gamma) + \cos \theta_D \sin \theta_A \cos(\beta + \gamma)} \quad (4)$$

These expressions match the implementation used in the processing code (with  $\gamma = 0$  for this study).

Assumptions and implications:

- $\beta$  interpretation:  $\beta$  is defined as an orbital-geometry term computed from orbit inclination and latitude (not DEM slope aspect). This matches the code implementation and avoids confusion with terrain aspect.
- $\gamma = 0$ : Assuming zero cross-track tilt is reasonable for the relatively flat dam area. For steep abutments,  $\gamma$  should be estimated from a DEM.
- IDW interpolation (DESC → ASC): Spatial interpolation introduces estimation error where data

are sparse. The chosen radius and neighbour selection mitigate this, but coherence masks and spatial distributions should be inspected.

- Sensitivity: Radar LOS is more sensitive to vertical motion than to east–west horizontal motion. Thus,  $d_V$  estimates are more robust, while  $d_H$  typically exhibits larger uncertainties.

Table 1: Summary of symbols and parameters used in the LOS decomposition.

Symbol	Meaning	Source in code	Comment
$d_{ASC}, d_{DESC}$	Line-of-sight (LOS) displacements from ascending and descending orbits	<code>disp, disp_idw</code> columns	Original InSAR data (ASC/DESC)
$\theta_A, \theta_D$	Incidence angle (between LOS and vertical)	<code>incidence_angle, theta_desc</code>	Retrieved from EGMS metadata
$\alpha_A, \alpha_D$	Azimuth angle of the satellite orbit (track angle)	<code>track_angle, alpha_desc</code>	Also obtained from EGMS metadata
$\beta$	Orbital geometric correction term (simplified)	<code>np.arcsin(...)</code> function	Not the surface aspect, but an approximate geometric factor
$\gamma$	Cross-track surface tilt	Set to 0	Assumes flat terrain
$d_V, d_H$	Vertical (U) and horizontal (E–W) displacements	Computed by trigonometric decomposition	Final results, compared with ORTHO data

This formulation ensures that displacements are correctly projected onto the vertical and horizontal reference frame, considering local terrain geometry. The decomposition was applied to each point within the dam area and aggregated into 100 m grid cells for subsequent comparison with the orthogonally derived displacements from the EGMS ORTHO products.

### Spatial aggregation into grid cells

The computed  $d_V$  and  $d_H$  components were aggregated into 100 m grid cells centered on the ORTHO points. This spatial aggregation ensured consistency between InSAR-derived components and independent orthogonal measurements and facilitated comparison across the dam body.

### Visualization and validation

Selected cells across the dam were analyzed in detail. For each cell, vertical and horizontal displacement time-series were plotted, comparing ASC/DESC LOS measurements, ASC/DESC IDW decomposed components, and ORTHO displacements.

#### 2.2.3 Validation with orthophoto-derived displacements

To evaluate the reliability of InSAR-derived displacements, both  $d_V$  and  $d_H$  components were compared to independent measurements obtained from orthophoto data.

For each displacement direction, pairs of co-located observations were extracted, resulting in two datasets:

- $d_V^{\text{InSAR}}$  vs.  $d_V^{\text{Ortho}}$
- $d_H^{\text{InSAR}}$  vs.  $d_H^{\text{Ortho}}$

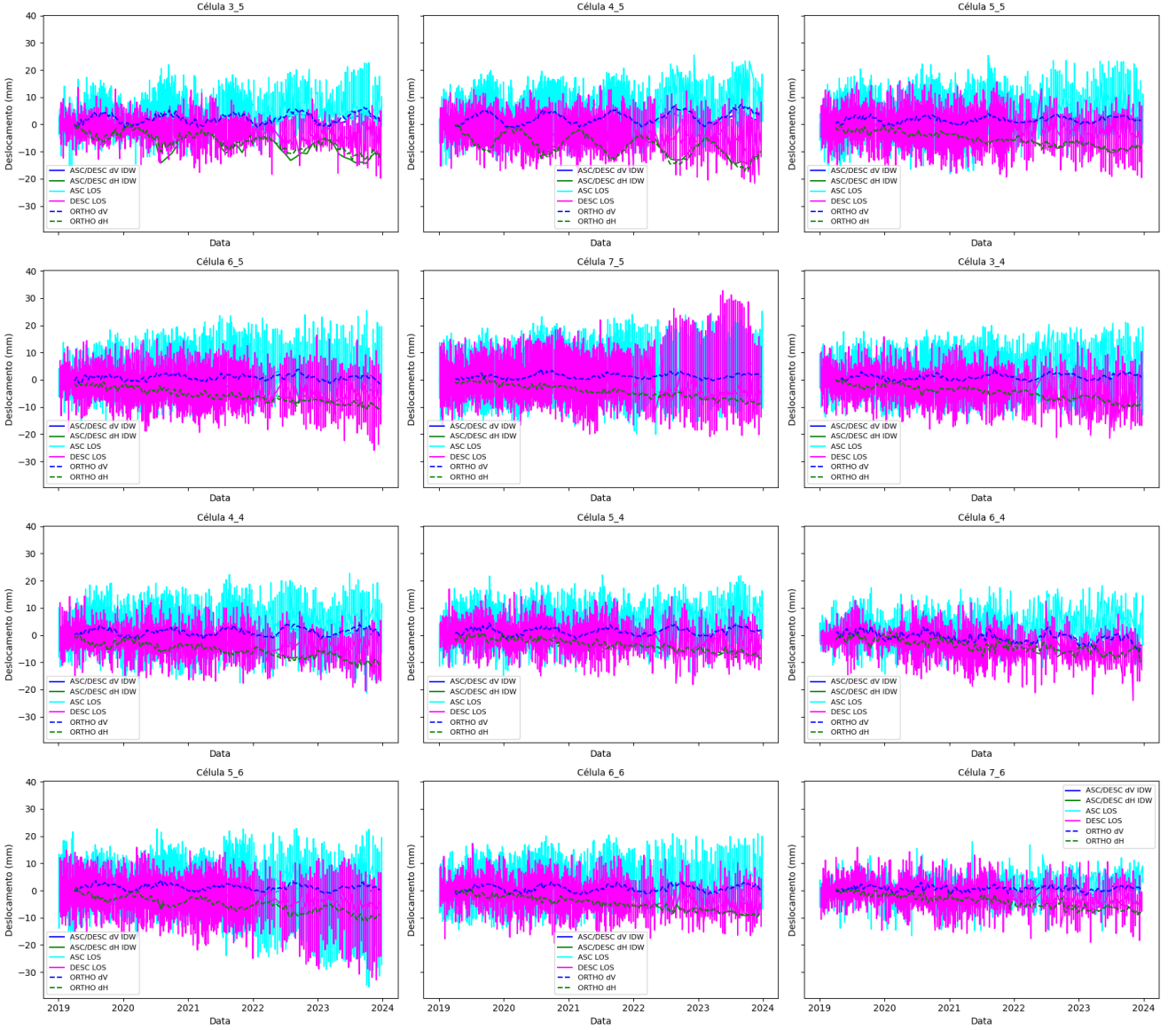


Figure 4: Extended plots including original ASC and DESC LOS measurements.

These datasets were analysed through scatter plots, and their correspondence was quantified using standard statistical metrics.

#### 2.2.4 Accuracy assessment metrics

The consistency between InSAR and Ortho displacements was evaluated using RMSE, MAE, and Pearson's  $r$ , measuring respectively the average error, absolute deviation, and linear correlation between datasets.

- Root Mean Square Error (RMSE):

$$\text{RMSE} = \sqrt{\frac{1}{n} \sum_{i=1}^n (y_i - \hat{y}_i)^2} \quad (5)$$

which measures the average magnitude of the error in millimetres.

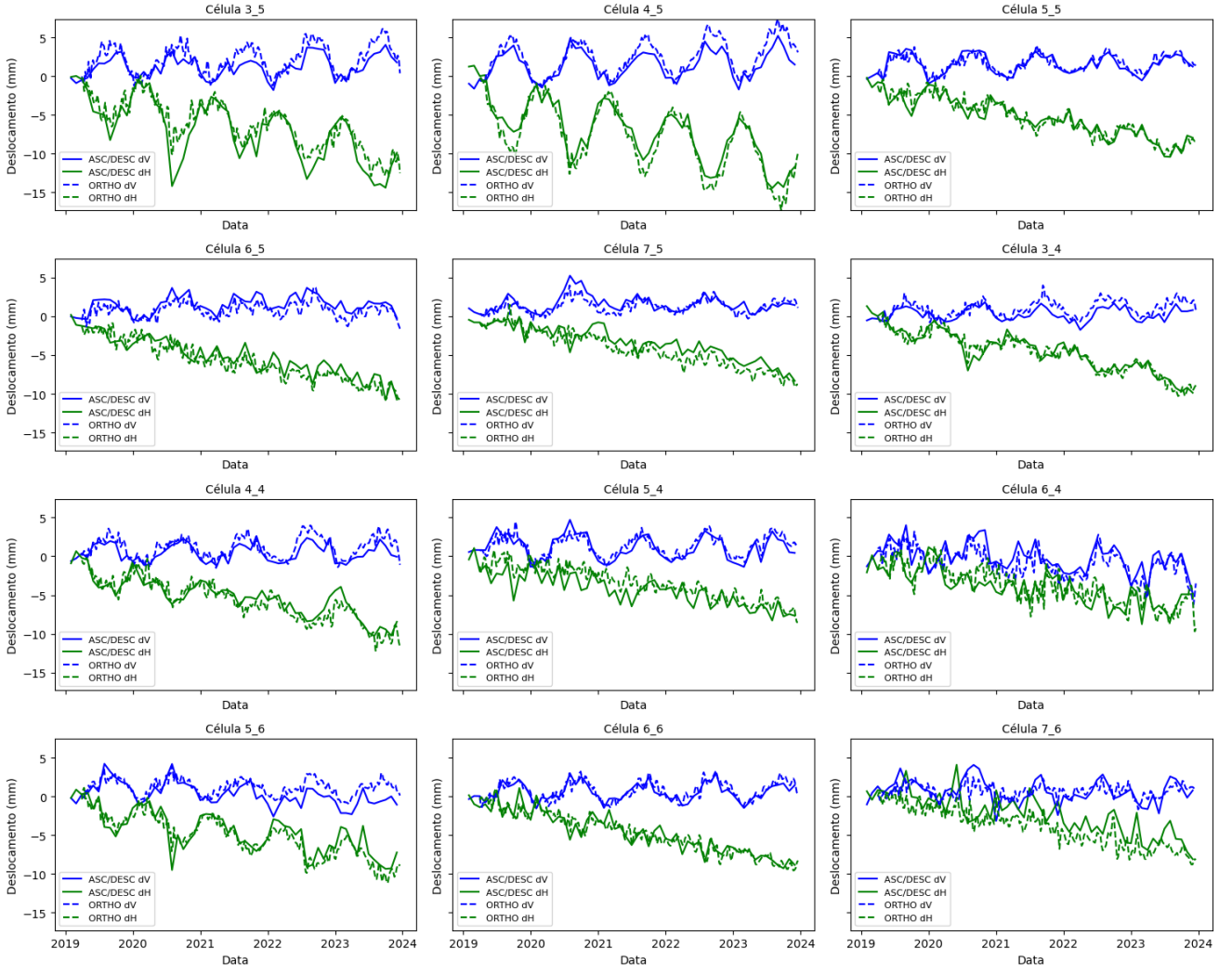


Figure 5: Time-series plots of dV and dH from ASC/DESC IDW compared to ORTHO.

- Mean Absolute Error (MAE):

$$\text{MAE} = \frac{1}{n} \sum_{i=1}^n |y_i - \hat{y}_i| \quad (6)$$

- Pearson Correlation Coefficient ( $r$ ):

$$r = \frac{\text{cov}(y_i, \hat{y}_i)}{\sigma_y \sigma_{\hat{y}}} \quad (7)$$

## 2.3 Clustering and Pattern Analysis

### 2.3.1 overview

Clustering techniques were applied to identify spatial and temporal patterns of deformation within the InSAR-derived displacement datasets. These unsupervised machine learning methods enable the grouping of areas with similar deformation behaviour, facilitating the identification of zones with homogeneous motion, potential structural anomalies, or early indicators of instability.

In this study, both spatial clustering (using average displacement values) and temporal clustering (using time-series of deformation) were implemented. The main algorithms adopted were K-Means and Hierarchical Clustering using DTW distance.

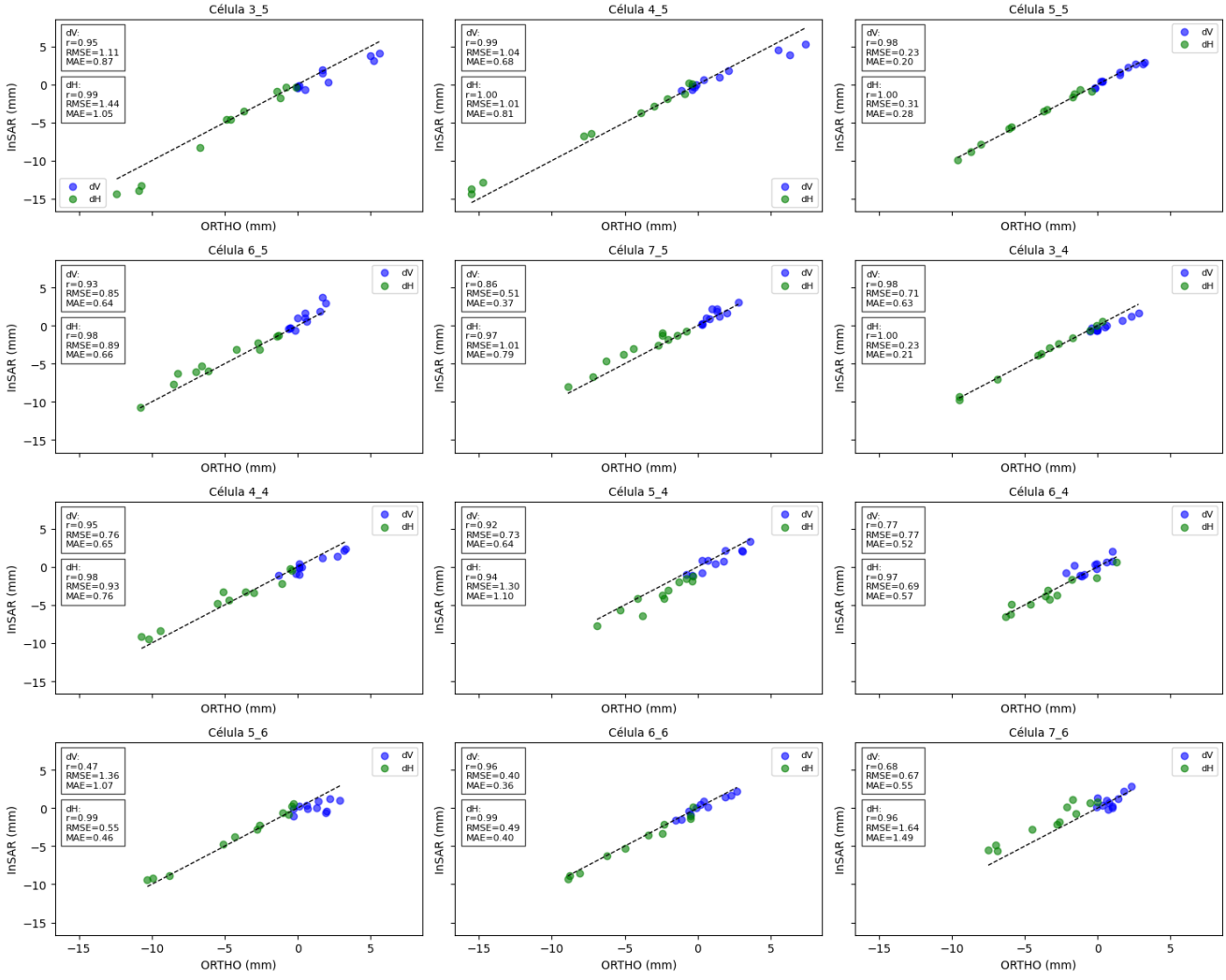


Figure 6: Plots showing line-identity comparison and statistical validation metrics.

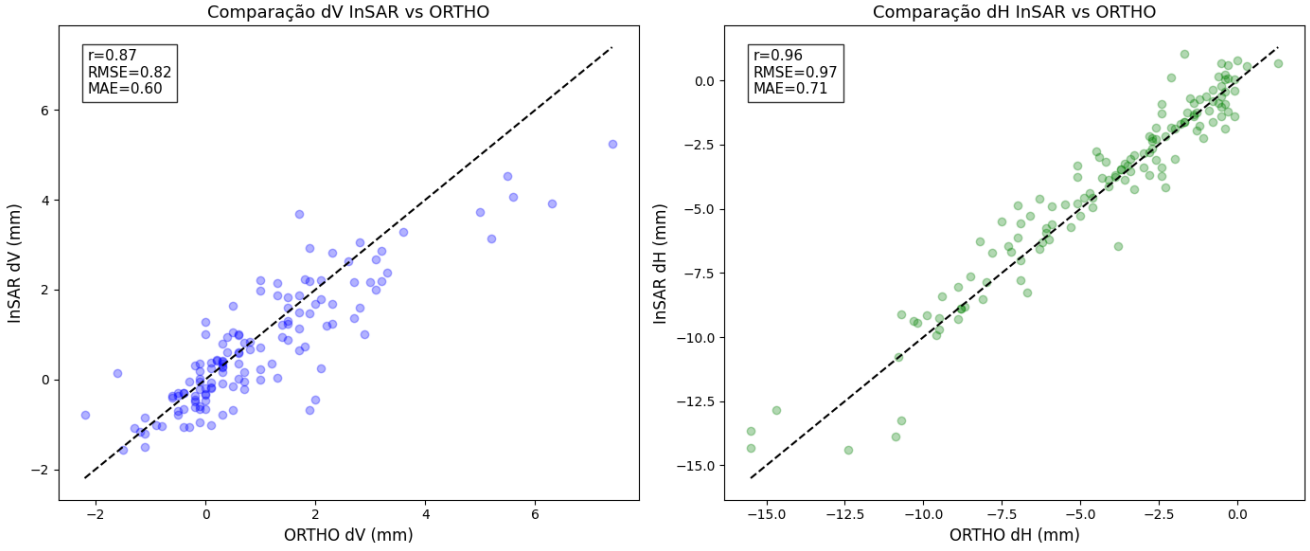


Figure 7: ....

### 2.3.2 K-Means Clustering

The K-Means algorithm was first employed to partition the InSAR displacement time-series into a predefined number of clusters based on their overall temporal similarity. This method minimizes intra-

cluster variance by iteratively assigning each time-series to the nearest cluster centroid and recalculating centroids until convergence. The optimal number of clusters was determined through the Silhouette Score and the Elbow Method, ensuring a balance between cluster compactness and separation. K-Means provided an efficient way to identify dominant deformation behaviours—such as stable, subsiding, or uplifting areas—serving as a first-level classification of the dataset.



(a) Study Area: Grid cells and InSAR observations. White points show the ortho points; colored points represent the processed ascending and descending orbit acquisitions combined.

(b) K-Means clustering results for vertical displacement (dV) time-series. Each color represents a cluster of grid cells with similar temporal deformation patterns.

Figure 8: Overview of the study area and cluster analysis.

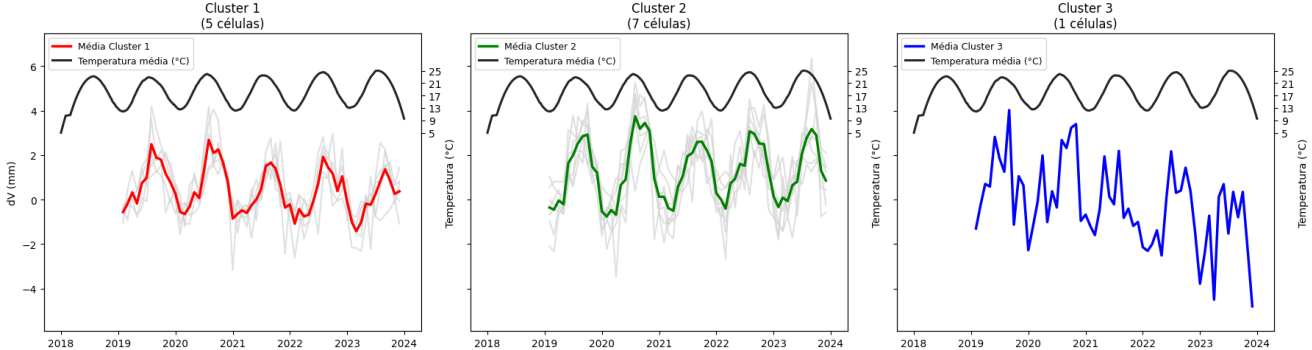


Figure 9: Mean vertical displacement (dV) per cluster with smoothed temperature (black line).

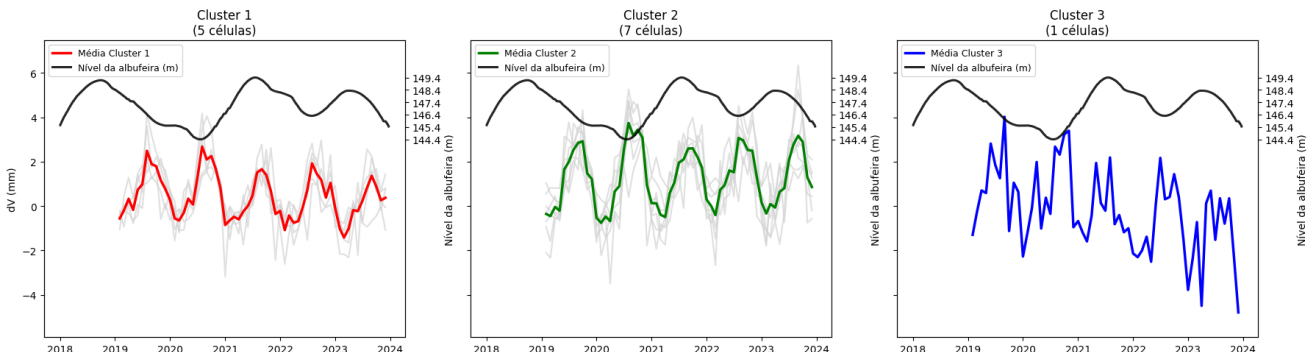


Figure 10: Mean vertical displacement (dV) per cluster with reservoir water level (black line).

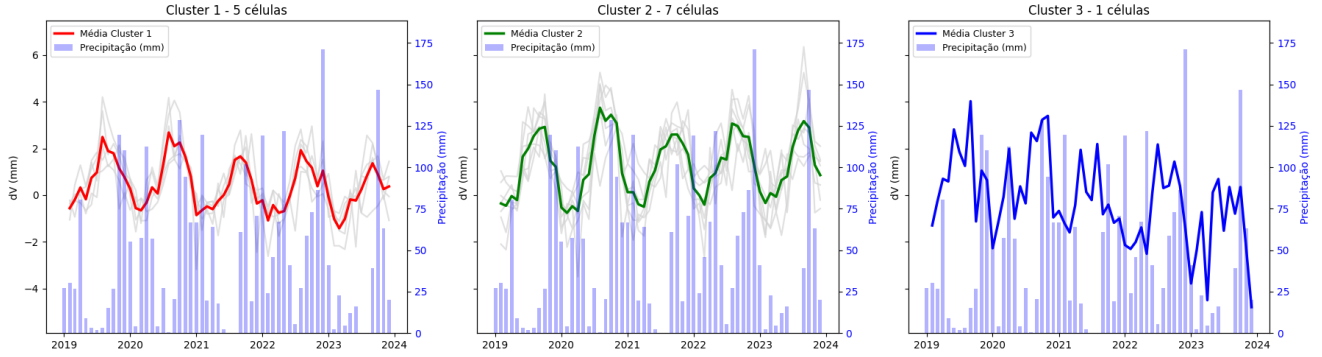


Figure 11: Mean vertical displacement ( $dV$ ) per cluster with precipitation (blue bars)

### 2.3.3 Hierarchical Clustering using DTW Distance

To complement the partition-based results of K-Means, Hierarchical Clustering using Dynamic Time Warping (DTW) distance was applied to further explore the nested relationships among deformation time-series. Unlike conventional Euclidean metrics, DTW accounts for time shifts and non-linear temporal variations, making it particularly suited for deformation signals influenced by seasonal or delayed processes.

DTW measures the similarity between two sequences  $X = (x_1, \dots, x_n)$  and  $Y = (y_1, \dots, y_m)$  by finding the optimal alignment path  $w$  that minimizes the cumulative distance:

$$\text{DTW}(X, Y) = \min_w \sum_{(i,j) \in w} \|x_i - y_j\| \quad (8)$$

The hierarchical algorithm begins by treating each time-series as an individual cluster and successively merges them based on their DTW-based distance, according to a chosen linkage criterion (e.g., average or Ward's method). The resulting dendrogram provides a visual representation of cluster hierarchy, revealing groups of time-series that share similar deformation dynamics. The dendrogram was cut at the level that maximized the Silhouette Score, ensuring well-separated and physically meaningful groupings.

This combined DTW–Hierarchical approach offered:

- A detailed visualization of relationships among deformation patterns,
- The ability to detect gradual transitions between deformation regimes, and
- Independent validation of the K-Means results.

### 2.3.4 Temporal Decomposition of Clustered Time-Series

To further explore the temporal dynamics of the displacement signals, STL decomposition was applied to the cluster-mean series from both K-Means and DTW-Hierarchical clustering. Trend, seasonal, and residual components are presented for each cluster.

Overall, the use of K-Means and DTW-based Hierarchical Clustering enabled a comprehensive understanding of deformation behaviour—from dominant regional trends to subtle local variations—supporting a more robust interpretation of the InSAR-derived displacement field.

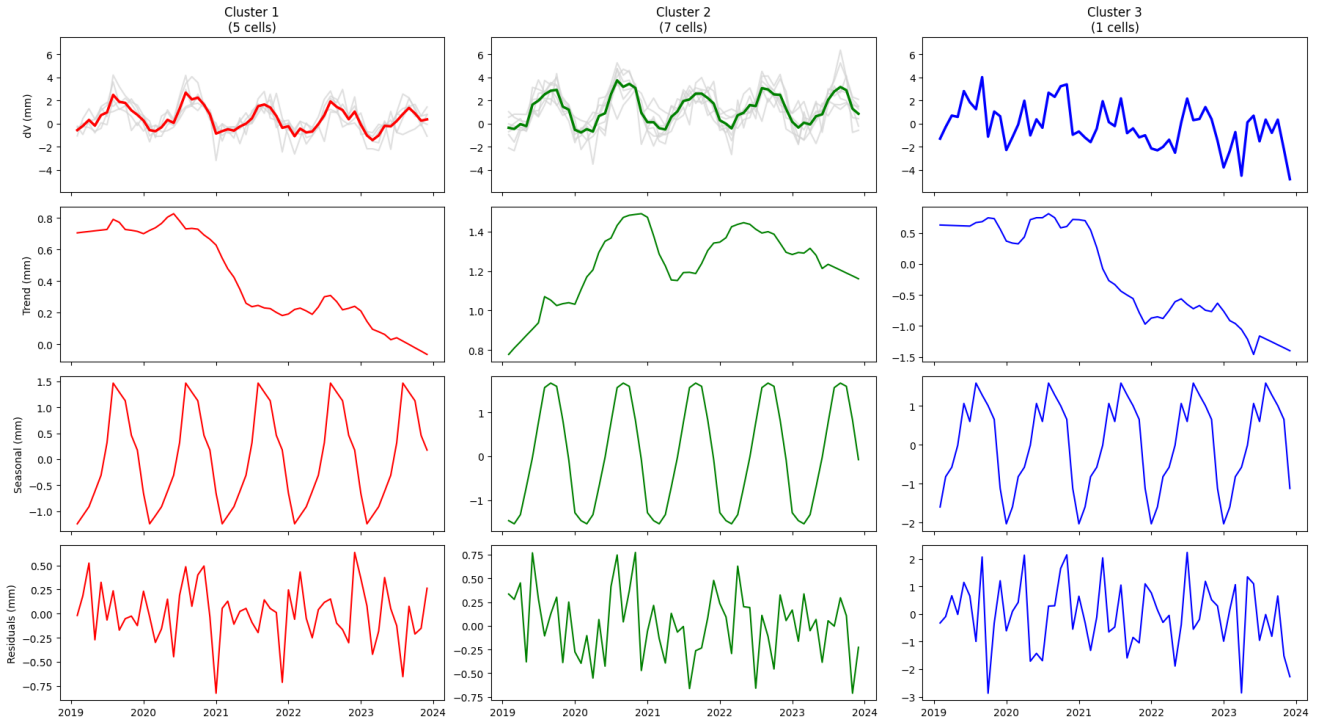


Figure 12: STL decomposition of mean vertical displacement ( $dV$ ) per cluster: trend (top), seasonal component (middle), residuals (bottom). Cluster colours correspond to K-Means results.

### 3 Conclusion

Summarize key points and future work.

### References

- Derauw, D., Nicolas, d., Jaspard, M., Caselli, A., & Samsonov, S. (2020). Ongoing automated ground deformation monitoring of Domuyo - Laguna del Maule area (Argentina) using Sentinel-1 MSBAS time series: Methodology description and first observations for the period 2015–2020. *Journal of South American Earth Sciences*, 104, 102850. <https://doi.org/10.1016/j.jsames.2020.102850>
- Giordano, P. F., Kamariotis, A., Giardina, G., Chatzi, E., & Limongelli, M. P. (2025). Uncertainty propagation in satellite InSAR data analysis for structural health monitoring. *Automation in Construction*, 177, 106371. <https://doi.org/10.1016/j.autcon.2025.106371>
- Hariri-Ardebili, M. A., Salamon, J., Mazza, G., Tosun, H., & Xu, B. (2020). Advances in Dam Engineering.
- Maes, H. (2025). Contribution of remote sensing to the monitoring of geotechnical structures: Case studies.
- Park, S.-W., & Hong, S.-H. (2021). Nonlinear Modeling of Subsidence From a Decade of InSAR Time Series. *Geophysical Research Letters*, 48(3), e2020GL090970. <https://doi.org/10.1029/2020GL090970>
- Roque, D., Falcão, A. P., Perissin, D., Amado, C., Lemos, J. V., & Fonseca, A. (2023). SARClust—A New Tool to Analyze InSAR Displacement Time Series for Structure Monitoring. *Sustainability*, 15(4), 3728. <https://doi.org/10.3390/su15043728>

- Salcedo-Sanz, S., Ghamisi, P., Piles, M., Werner, M., Cuadra, L., Moreno-Martínez, A., Izquierdo-Verdiguier, E., Muñoz-Marí, J., Mosavi, A., & Camps-Valls, G. (2020). Machine Learning Information Fusion in Earth Observation: A Comprehensive Review of Methods, Applications and Data Sources. *Information Fusion*, 63, 256–272. <https://doi.org/10.1016/j.inffus.2020.07.004>
- Schlögl, M., Widhalm, B., & Avian, M. (2021). Comprehensive time-series analysis of bridge deformation using differential satellite radar interferometry based on Sentinel-1. *ISPRS Journal of Photogrammetry and Remote Sensing*, 172, 132–146. <https://doi.org/10.1016/j.isprsjprs.2020.12.001>
- Simoes, R., Camara, G., Queiroz, G., Souza, F., Andrade, P. R., Santos, L., Carvalho, A., & Ferreira, K. (2021). Satellite Image Time Series Analysis for Big Earth Observation Data. *Remote Sensing*, 13(13), 2428. <https://doi.org/10.3390/rs13132428>
- Sousa, J. J., Liu, G., Fan, J., Perski, Z., Steger, S., Bai, S., Wei, L., Salvi, S., Wang, Q., Tu, J., Tong, L., Mayrhofer, P., Sonnenschein, R., Liu, S., Mao, Y., Tolomei, C., Bignami, C., Atzori, S., Pezzo, G., ... Peres, E. (2021). Geohazards Monitoring and Assessment Using Multi-Source Earth Observation Techniques. *Remote Sensing*, 13(21), 4269. <https://doi.org/10.3390/rs13214269>
- Tomás, R., & Li, Z. (2017). Earth Observations for Geohazards: Present and Future Challenges. *Remote Sensing*, 9(3), 194. <https://doi.org/10.3390/rs9030194>
- Tu, K., Ye, S., Zou, J., Hua, C., & Guo, J. (2023). InSAR Displacement with High-Resolution Optical Remote Sensing for the Early Detection and Deformation Analysis of Active Landslides in the Upper Yellow River. *Water*, 15(4), 769. <https://doi.org/10.3390/w15040769>